Nanoscale

PAPER

View Article Online
View Journal

Cite this: DOI: 10.1039/d4nr00727a

An optimized metastructure switchable between ultra-wideband angle-insensitive absorption and transmissive polarization conversion: a theoretical study

Zhao Tang, You-Ran Wu, Si-Ying Li and Hai-Feng Zhang *

An optimized metastructure (MS) switchable between ultra-wideband (UWB) angle-insensitive absorption, and transmissive linear-to-circular (LTC) polarization conversion (PC), is proposed, which is a theoretical study. The structural parameters of this MS are optimized by the thermal exchange optimization algorithm. By modulating the chemical potential (μ_c) of the graphene-based hyperbolic metamaterial embedded in the MS, the MS can achieve UWB absorption in the absorption state and LTC PC in the transmission state. At normal incidence, in the absorption state, the MS exhibits absorptivity exceeding 0.9 within 7–15.45 THz, with a relative bandwidth (RBW) of 75.28%. By elevating μ_c, an UWB LTC PC is realized, with a RBW of 118.8%, achieving transmittance above 0.9 and the axial ratio below 3 dB. When prioritizing the angular stability, in the absorption state, the MS secures the angular stability of 75° for TE waves and 65° for TM ones. In the transmission state, the angular stability of PC reaches 60°, with RBW = 100.7%. Moreover, by manipulating μ_c, the tunability of UWB absorption is realized. The optimized MS provides a reference for designing multifunctional intelligent terahertz modulators, with promising application potential in domains like electromagnetic shielding, communication systems, and THz modulation.

Received 21st February 2024,
Accepted 4th April 2024

DOI: 10.1039/d4nr00727a

rsc.li/nanoscale

1. Introduction

Electromagnetic waves (EWs) are a form of electromagnetic radiation, which have various propagation modes. The spectra of EWs encompass a broad range of wavelengths, including microwave, terahertz (THz) band, and visible light, and others. The THz band is particularly noteworthy, which, owing to its strong penetration capability and vast potential for future applications, holds significant value in fields such as imaging,[1–3] security monitoring,[4,5] and communication technologies.[6,7] Due to the abundant utilization potentiality of THz waves, in recent years, there has been a surge of interest in manipulating and controlling THz waves in terms of amplitude, phase, polarization states, and other aspects.[8] However, the natural world lacks materials that naturally interact with THz waves, rendering the manipulation of them a challenging endeavor. To address this huedle, metastructure (MS) has been proposed, which is an artificial medium topology structure.[9] Through the precise design of the microstructure, MS is able to precisely control the EWs. Consequently, the advent of MS has opened new avenues for exploring and utilizing THz waves. THz absorbers[10] and polarization converters[11] stand out as potent tools enabling precise control and manipulation of THz waves.

Absorbers can absorb the energy of EWs, which holds significant value in domains like military stealth and addressing electromagnetic pollution. In recent years, numerous types of THz absorbers have been proposed, encompassing ultra-wideband (UWB) absorbers,[12–14] dual-band absorbers,[15,16] and multi-band absorbers,[17,18] among others. In response to the increasingly intricate electromagnetic environment, the demands for UWB absorbers in terms of bandwidth and angular stability of incident angle are progressively escalating. In 2021, Wu *et al.* presented a dynamically tunable THz UWB absorber based on vanadium dioxide (VO_2).[19] At vertical incidence, the relative bandwidth (RBW) with absorptivity surpassing 0.9 reached 82.7%. Moreover, for both the transverse electric (TE) and transverse magnetic (TM) waves, the angular stability reached 55°, yet the corresponding absorption threshold was merely 0.75. In 2022, Wang *et al.* introduced an asymmetric T-shaped resonator, achieving an absorptivity exceeding 80% with a RBW of 31.69%.[20] However, the angular stability of this absorber was not investigated. In summary,

College of Electronic and Optical Engineering & College of Flexible Electronics (Future Technology), Nanjing University of Posts and Telecommunications, Nanjing, 210023, China. E-mail: hanlor@163.com, hanlor@njupt.edu.cn

there is a multitude of absorbers in the THz band currently available. However, currently, issues persist regarding insufficient absorption bandwidth and limited angular stability.

Polarization converters can manipulate polarization states and hold significant potential in fields like circularly polarized antennas,[21,22] antenna radomes,[23] and sensors.[24,25] With the advancement of communication technology, traditional linearly polarized antennas face challenges in terms of susceptibility to interference and stringent requirements on the direction of the incident EWs, making them less suitable for practical applications. Circularly polarized waves (CPWs), on the other hand, possess unique advantages like low sensitivity to multiple paths, and atmospheric effects of absorption and reflection. This has led to increasing adoption of CPWs in both civilian and military applications, prompting a surge of interest in developing linear-to-circular (LTC) polarization converters. LTC polarization converters, designed to transform linearly polarized waves into CPWs, can be broadly classified into two main categories: reflective type[26–28] and transmissive type.[29–32] The reflective polarization converters often encounter challenges such as mixing reflected CPWs with incident linearly polarized waves, as well as a signal blockage in the feed. On the other hand, transmissive LTC polarization converters can effectively address these issues, making them a focal point of research in recent years.

In 2020, Arnieri *et al.* introduced a LTC polarization converter, which achieved PC with a transmittance exceeding 0.9 and maintained the angular stability up to 50°.[30] However, its operational frequency range is limited to 17.6–22.4 GHz, with a RBW of only 24%. In the same year, Hou *et al.* proposed an all-dielectric device capable of achieving transmissive LTC PC within 0.555–0.737 THz with a RBW of 28.17%, and consideration for angular stability was absent.[31] In 2022, Wu *et al.* introduced a double-layer structure, enabling LTC PC within 0.46–0.62 THz, accompanied by a transmittance exceeding 0.82 and RBW = 29.6%.[32] However, the study did not explore the angular stability. Overall, existing transmissive polarization converters continue to grapple with challenges related to limited transmittance, operational bandwidth, and angular stability.

The absorbers and polarization converters mentioned above, due to their single functionality and fixed operational frequencies, struggle to meet the escalating requirements for modulating EWs. As THz technology advances and working environments become more intricate, the prevailing direction of modulating THz is to devise tunable devices that offer multifunctional integration.[33,34] In pursuit of achieving multifunctional integration in THz devices, researchers have been exploring the incorporation of active photonic materials, such as black phosphorus,[35,36] liquid crystal,[37,38] VO_2,[39,40] and graphene.[41,42] The properties of these materials can be modulated through the application of an external excitation field, enabling the reconfigurability of the device. In 2020, Yan *et al.*[33] introduced a switchable device based on VO_2, incorporating both UWB absorption and LTC PC. In absorption state, the proposed device exhibited absorption properties within 0.74–1.62 THz. The corresponding absolute bandwidth (AB) and RBW are 0.87 THz and 75% respectively. However, the study solely addressed the angular stability of the incident angle under the TE mode, which was only 35°. In reflective state, a reflective LTC PC is realized. The AB of PC was only 0.8 THz, and the corresponding RBW reached 42.7%. The angular stability was maintained at 50°. Furthermore, graphene-based hyperbolic metamaterial (GHM) serves as a type of uniform medium with hyperbolic dispersion and anisotropic dielectric constants. It can generate surface currents that confine incident EWs within the structure, thereby exhibiting the capability to absorb EWs.[43,44] Moreover, the chemical potential (μ_c) of the GHM can be effectively modulated by applying a bias voltage, thus altering their absorption characteristics.[45] This tunability paves the way for achieving the reconfigurability of GHM-based devices. In the current state, the designs that integrate UWB large-angle absorption, and transmissive LTC PC are relatively scarce.

In this paper, a switchable MS that incorporates GHM is proposed. Through the application of a bias voltage to modulate the μ_c of GHM, the MS gains the versatility to transition between absorption and transmission states, consequently integrating the functionalities of UWB large-angle absorption and transmissive LTC PC. The structural parameters of the MS play a pivotal role in influencing its performance. The conventional design approach involves creating multiple versions with different structural parameter sets and then comparing metrics like bandwidth to determine the optimal configuration. While the design experience of researchers can reduce the number of design iterations, manual parameter selection often lacks precision, resulting in suboptimal choices. This study harnesses the thermal exchange optimization (TEO) algorithm,[46] pioneered by Kaveh *et al.* in 2017. This algorithm, drawing inspiration from Newton's cooling law, boasts various strengths such as superior accuracy, rapid convergence, and robustness. It is utilized to propel the transfer matrix method (TMM),[47] fine-tuning the values of permittivities and thicknesses of dielectrics within the MS, alongside optimizing the μ_c of the GHM. The TEO algorithm presents a promising avenue for automating the configuration of structural parameters within the MS. This can significantly streamline the design process, and alleviate the costs associated with trial and error. For the optimized MS, considering only normal incidence, in absorption state, the UWB absorption interval with an absorptivity exceeding 0.9 spans from 7 to 15.45 THz, with AB = 8.45 THz and RBW = 75.28%. By altering the μ_c of the GHM, the MS transitions into the transmission state. Within 3.9–15.32 THz, an UWB LTC PC is achieved, manifesting an associated AB of 11.42 THz and a RBW of 118.8%. Delving further, the angular stability of both absorption and PC in the MS is taken into account. In the absorption state, an UWB absorption within 8.9–13.1 THz is achieved, showcasing a RBW of 38.2%. Notably, the angular stability for TE and TM waves stands at 75° and 65°, respectively. In the transmission state, an impressive RBW of 100.7% for UWB PC within 4.37–13.23 THz is realized, with the angular stability reaching 60°, demonstrating excellent performance in terms of angular stability. Furthermore, the theory of impedance matching is

introduced to elucidate the physical mechanism of UWB absorption. By scrutinizing the distribution of electric field and impacts of periodicity number on MS's performance, the roles of each sequence within the MS are investigated. Finally, the tunability of UWB absorption is realized by adjusting the μ_c of the GHM in the MS. The proposed MS offers a range of advantages, including multifunctionality, wide operating frequency range, decent angular stability, and flexible controllability. It provides valuable insights for developing intelligent and multifunctional THz devices and holds immense application prospect in domains such as THz modulation, communication systems, and electromagnetic shielding.

2. Model construction and theory

2.1 The configuration of the MS

Fig. 1(a) presents a frontal view of the incident mode of the EWs entering this MS. The electric field orientation of the incident EWs aligns parallel to the x–y plane and forms a 45° angle with the +x-axis. Therefore, the electric field can be resolved into two mutually orthogonal components: E_x and E_y, which respectively align with the +x-axis and +y-axis, and correspond to the TE and TM waves.[48] This signifies that the incident EWs are linearly polarized. The depicted configuration of the proposed MS is presented in Fig. 1(b), which comprises dielectric A, air layer (B), GHM, and indium antimonide (D). The GHM, composed of medium C and graphene is abbreviated as G in the sequence for simplicity. The composite materials are arranged in a periodic sequence of $(GBGBG)^{N_1}$-$(AD)^{N_2}$ to form this versatile MS, where N_1 and N_2 respectively represent the number of unit sequences (GBGBG) and (AD). The EWs and coordinate axes are depicted in Fig. 1(b). The direction of the +z-axis signifies the incident trajectory and outgoing propagation direction of the EWs. θ represents the incident angle.

Without loss of generality, the structure is placed in air and the working temperature T_e (see eqn (1)) is 300 K. The thick-

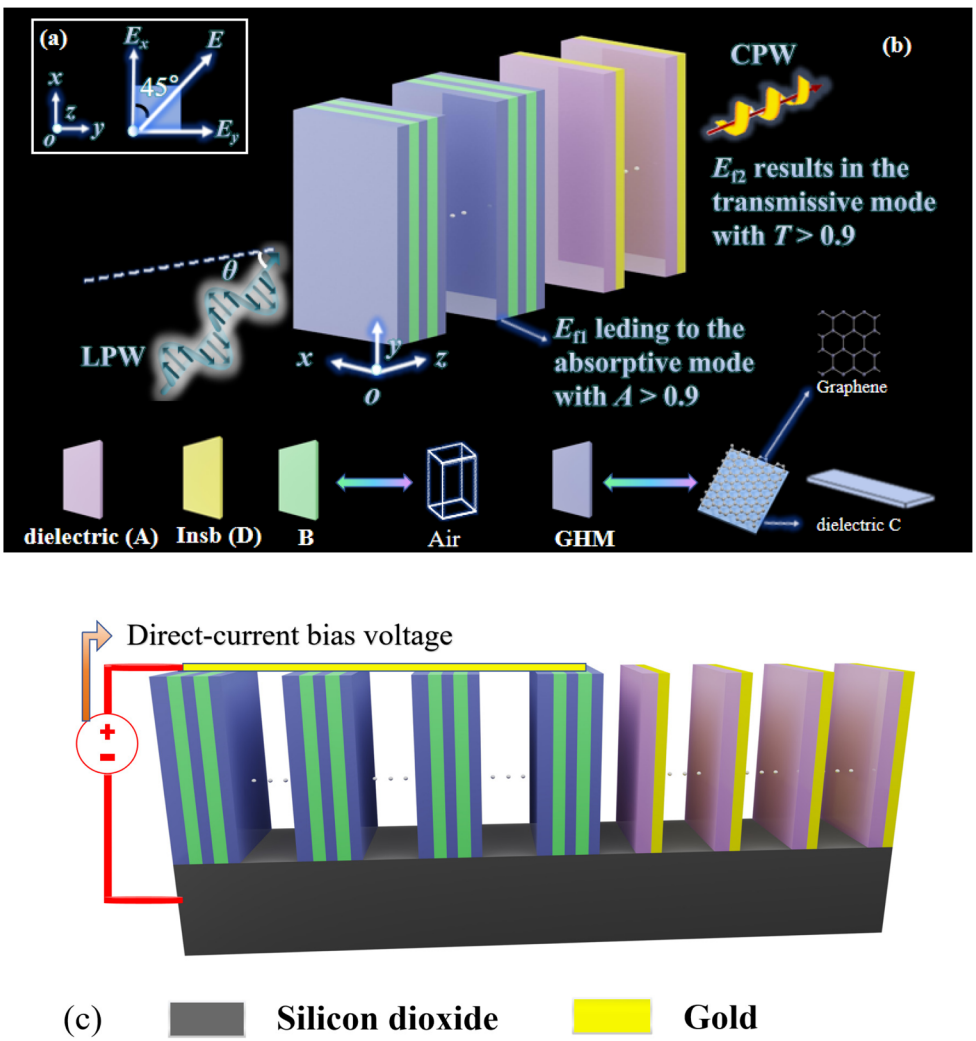

Fig. 1 (a) A front view of the incident mode of the EWs entering the MS. (b) The schematic configuration of this proposed MS. (c) The schematic diagram of GHM voltage application.

nesses of the mediums A, B, C, and D are severally symbolized as d_A, d_B, d_C, and d_D. Meanwhile, the permittivities of A and C are denoted as ε_A and ε_C. Additionally, the μ_c of GHM embedded in the proposed MS in absorption and transmission states are denoted as μ_{c_1} and μ_{c_2} respectively. All these variables are considered as independent variables in the objective function and are optimized by TEO. However, in that N_1 and N_2 are discrete and positive integers, which contradicts the continuous search space of TEO, the values of N_1 and N_2 are determined through an exhaustive method. This can substantially decrease the computational burden during the optimization process and afford an opportunity to assess the influence of the period numbers on the performance. Furthermore, the feed pattern of the GHM layers is illustrated in Fig. 1(c). In Fig. 1(c), the proposed MS is positioned on a silicon dioxide substrate. The top of the $(GBGBG)^{N_1}$ sequence has a direct connection to the gold electrode. A positive bias voltage bias voltage is applied to the gold electrodes, while a negative voltage is applied to the silicon dioxide substrate. Through this approach, the application of a bias voltage effectively allows for the modulation of the GHM's μ_c.[49–51]

2.2 The calculation of the TMM

Graphene, due to its ability to support surface plasmon excitations at THz frequencies, has emerged as an ideal material for absorbing THz waves. The inter-band and intra-band conductivities of the graphene, are donated as σ_g^{inter} and σ_g^{intra} respectively, and can be computed utilizing the Kubo formula,[52,53] represented by eqn (1) and (2):

$$\sigma_g^{intra} = \frac{ie^2 k_B T_e}{\hbar^2 \pi\left(\omega + \frac{i}{\tau}\right)}\left(\frac{\mu_c}{k_B T_e} + 2\ln\left(e^{\frac{-\mu_c}{k_B T_e}} + 1\right)\right), \quad (1)$$

$$\sigma_g^{inter} = i\frac{e^2}{4\pi\hbar}\ln\left|\frac{2\mu_c - \hbar(\omega + i/\tau)}{2\mu_c - \hbar(\omega + i/\tau)}\right|, \quad (2)$$

here e represents the electron charge, $\hbar$ denotes the reduced Planck constant, and k_B stands for the Boltzmann constant. ω is the angular frequency of incident EWs, and τ is the phenomenological scattering rate, which is 10^{-13} s. Subsequently, the electrical conductivity (σ_g) of graphene can be described by eqn (3):[52,53]

$$\sigma_g = \sigma_g^{inter} + \sigma_g^{intra}. \quad (3)$$

Based on the Kubo model, the effective dielectric constant, ε_G, can be expressed as shown in eqn (4):[52,53]

$$\varepsilon_G = 1 + \frac{i\sigma_g}{\omega\varepsilon_0 d_G}. \quad (4)$$

In this equation, ε_0 denotes the vacuum permittivity, and d_G represents the thickness of graphene, which is nm.[54] Different from conventional graphene-based materials, GHM possesses anisotropic characteristics with uniaxial dielectric tensor components. These components can be approximated written as eqn (5)–(7):[55]

$$\varepsilon = \begin{bmatrix} \varepsilon_x & 0 & 0 \\ 0 & \varepsilon_y & 0 \\ 0 & 0 & \varepsilon_z \end{bmatrix}, \quad (5)$$

$$\varepsilon_x = \varepsilon_y = \varepsilon_\parallel = \frac{\varepsilon_G d_G + \varepsilon_C d_C}{d_G + d_C}, \quad (6)$$

$$\varepsilon_z = \varepsilon_\perp = \frac{\varepsilon_G \varepsilon_C (d_G + d_C)}{d_G + d_C}, \quad (7)$$

where $\varepsilon_\parallel$ and $\varepsilon_\perp$ represent the parallel and perpendicular components of the permittivity of GHM respectively. According to Snell's law, the refractive index at an incident angle θ can be expressed as eqn (8):[56]

$$n_g = \sqrt{\frac{\varepsilon_\perp^2}{\varepsilon_\parallel} - \frac{\varepsilon_\perp}{\varepsilon_\parallel}\left(1 - \frac{\varepsilon_\parallel}{\varepsilon_\perp}\right)\sin^2\theta}. \quad (8)$$

For the anisotropic indium antimonide (InSb), the equation for the dielectric constant is displayed as eqn (9):[47]

$$\hat{\boldsymbol{\varepsilon}}_i = \begin{pmatrix} \varepsilon_{xx} & 0 & j\varepsilon_{xz} \\ 0 & \varepsilon_{yy} & 0 \\ -j\varepsilon_{xz} & 0 & \varepsilon_{xx} \end{pmatrix}, \quad (9)$$

where the components ε_{xx}, ε_{xz}, and ε_{yy} can be expressed as eqn (10):[47]

$$\begin{cases} \varepsilon_{xx} = \varepsilon_\infty\left(1 - \dfrac{{\omega_p}^2(\omega + j\nu)}{\omega[(\omega + j\nu)^2 - {\omega_c}^2]}\right) \\ \varepsilon_{xz} = \varepsilon_\infty \dfrac{-{\omega_p}^2\omega_c}{\omega[(\omega + j\nu)^2 - {\omega_c}^2]} \\ \varepsilon_{yy} = \varepsilon_\infty\left(1 - \dfrac{{\omega_p}^2}{\omega(\omega + j\nu_c)}\right) \end{cases}. \quad (10)$$

Here, ω_p represents the plasma frequency, defined as $Ne^2/(\varepsilon_0 m^*)$. $\nu = 10^{-6}\omega_p$ denotes the plasma collision frequency.[57] ω_c stands for the cyclotron frequency. N is a function of temperature T_e, and its calculation is shown as eqn (11):[47]

$$N = 5.76 \times 10^{14} T_e e^{\frac{-1.5072\times10^{-7}}{T_e}}. \quad (11)$$

When incident EWs are under TE and TM modes respectively, the dielectric constant of InSb exhibits certain differences, as shown in eqn (12) and (13):[47]

$$\varepsilon_D^{TE} = \varepsilon_{yy}, \quad (12)$$

$$\varepsilon_D^{TM} = \frac{{\varepsilon_{xx}}^2 - {\varepsilon_{xz}}^2}{\varepsilon_{xx}}. \quad (13)$$

In this paper, the TMM is employed to calculate the transmission characteristic of EWs through the MS. For dielectrics A, B, and GHM, the transfer matrix at the ith layer can be represented as eqn (14):[47]

$$\boldsymbol{M}_i = \begin{bmatrix} \cos\delta_i & -\frac{j}{\eta_i}\sin\delta_i \\ -j\eta_i\sin\delta_i & \cos\delta_i \end{bmatrix}, \quad (i = A, B, GHM), \quad (14)$$

where δ_i and η_i respectively represent the phase thickness and admittance of the ith layer medium. They are the functions of the dielectric constant ε_i and thickness d_i of the ith layer material, and the specific calculation equations of δ_i and η_i can be found in ref. 48.

InSb exhibits a transfer matrix under TE mode that aligns with that of conventional mediums. However, due to its anisotropy under TM mode, the transfer matrix for InSb experiences alteration, represented as eqn (15):[47]

$$\begin{cases} M_{\mathrm{D}}^{\mathrm{TM}} = \begin{pmatrix} m_{11} & m_{12} \\ m_{21} & m_{22} \end{pmatrix}, \\ m_{11} = \cos(k_z d_{\mathrm{D}}) + \dfrac{k_x \varepsilon_{xz}}{k_z \varepsilon_{xx}} \sin(k_z d_{\mathrm{D}}), \\ m_{12} = -\frac{j}{\eta^{\mathrm{TM}}} \left[1 + \left(\dfrac{k_x \varepsilon_{xz}}{k_z \varepsilon_{xx}} \right)^2 \right] \sin(k_z d_{\mathrm{D}}), \\ m_{21} = -j\eta^{\mathrm{TM}} \sin(k_z d_{\mathrm{D}}), \\ m_{22} = \cos(k_z d_{\mathrm{D}}) - \dfrac{k_x \varepsilon_{xz}}{k_z \varepsilon_{xx}} \sin(k_z d_{\mathrm{D}}). \end{cases} \tag{15}$$

The methods for calculating k_z, k_x are detailed in ref. 48. Eventually, the overall transfer matrix of the MS is represented as eqn (16):[47]

$$\boldsymbol{M}_{\mathrm{total}} = \prod_{i=1}^{5 \cdot N_1 + 2 \cdot N_2} \boldsymbol{M}_i = \begin{bmatrix} m_{11} & m_{12} \\ m_{21} & m_{22} \end{bmatrix}. \tag{16}$$

Subsequently, the calculation of the transmission and reflection coefficients of the incident EWs passing through the MS, which are denoted as t and r respectively, can be found in ref. 47. For the incident EWs, the transmittance (T) is represented as $T = |t|^2$, while the reflectance (R) is denoted as $R = |r|^2$. The absorptivity, denoted as A, can be calculated as $A = 1 - R - T$. In this study, the absorptivity for TE and TM waves are severally denoted as A_{TE} and A_{TM}, and both of them greater than 0.9 is considered the threshold for ideal absorption.[58]

Significantly, the transmission coefficient also takes the form $t = |t|e^{j\varphi}$, where φ denotes the phase of the transmitted EWs. For TE and TM waves, these phases are denoted as φ_{TE} and φ_{TM}, respectively. Consequently, the phase difference ($\Delta\varphi$) between these two waves can be calculated as $\Delta\varphi = \varphi_{\mathrm{TM}} - \varphi_{\mathrm{TE}}$. Then, the AR, employed to discern the polarization state of the EWs, is expressed as eqn (17):[59]

$$\mathrm{AR} = \sqrt{\frac{|T_{\mathrm{TE}}|^2 + |T_{\mathrm{TM}}|^2 + \sqrt{a}}{|T_{\mathrm{TE}}|^2 + |T_{\mathrm{TM}}|^2 - \sqrt{a}}}, \tag{17}$$

$$a = |T_{\mathrm{TE}}|^4 + |T_{\mathrm{TM}}|^4 + 2 \cdot |T_{\mathrm{TE}}|^2 \cdot |T_{\mathrm{TM}}|^2 \cdot \cos(2\Delta\varphi), \tag{18}$$

where T_{TE} and T_{TM} correspondingly denote the transmittance of TE and TM waves. A transmitted wave is regarded as circularly polarized when the AR is less than 3 dB.[59] In this paper, both T_{TE} and T_{TM} exceed 0.9, with AR less than 3 dB, signifying the desired achievement of efficient transmissive LTC PC.

2.3 The introduction of the TEO algorithms

The specific workflow is illustrated in Fig. 2. Firstly, similar to other intelligent *meta*-heuristic algorithms, the population coordinates, representing the initial temperatures of the agents, are initialized in the search space, by eqn (19):[46]

$$T_i^0 = T_{\min} + \mathrm{ran} \cdot (T_{\max} - T_{\min}). \tag{19}$$

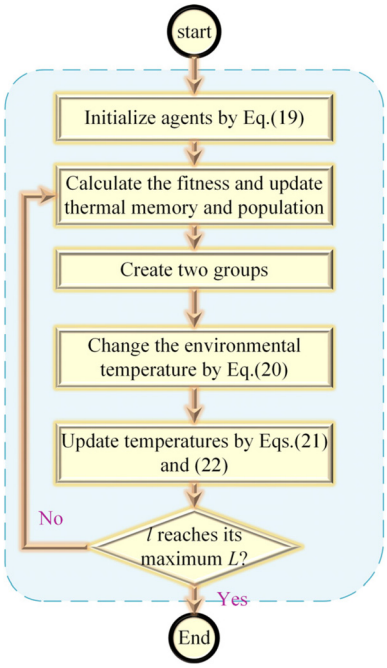

Fig. 2 The working flow of TEO algorithm.

In eqn (19), i represents the ith individual, $T_{\min}$ and $T_{\max}$ are the lower and upper bounds, respectively, for the variables to be optimized, and ran is a random value between 0 and 1. Next, the fitness of all individuals is calculated using the objective function, and the current best solution and cost are stored in the thermal memory. Then, all individuals are divided into two groups: the cooling object group and the environmental group. The environmental temperature is updated using eqn (20):[46]

$$T_i^{\mathrm{env}} = (1 - (c_1 + c_2 \cdot (1 - t)) \cdot \mathrm{ran}) \cdot T_i^{\mathrm{env}'}, \tag{20}$$

where T_i^{env} is the updated environmental temperature, and c_1 and c_2 signify control variables. $T_i^{\mathrm{env}'}$ represents the precious temperature of the environment, and $t = l/L$, where l denotes the current iteration number, and L is the maximum number of iterations. Based on the principles of heat exchange from physics, the temperature of all objects is updated according to eqn (21):[46]

$$T_i^{\mathrm{new}} = T_i^{\mathrm{env}} + (T_i^{\mathrm{old}} - T_i^{\mathrm{env}}) e^{-\beta t}. \tag{21}$$

Here, T_i^{new} represents the updated temperature of the object, while T_i^{old} stands for the previous temperature of the object. The symbol β signifies the ratio between the current individual's temperature and the population's lowest temperature. Therefore, individuals with lower costs have smaller β values, resulting in smaller changes in their positions. However, this may lead to getting trapped in local optima. To prevent falling into that, a parameter Pro is introduced, which determines whether to modify a specific element in an agent's position vector. If ran < Pro, then a random dimension of the

*i*th individual is selected, and its value is mutated according to eqn (22):[46]

$$T_{i,j} = T_{i,\min} + \mathrm{ran} \cdot (T_{j,\max} - T_{j,\min}), \quad (22)$$

where, $T_{i,j}$ is the *j*th variable of the *i*th individual. $T_{j,\max}$ and $T_{j,\min}$ severally represent the upper and lower bounds of the *j*th variable. Finally, it is checked whether the maximum iteration count has been reached. If not, the updating loop continues.

3. The results and verification

Firstly, only considering the normal incidence (θ = 0°), the structural parameters of the MS are optimized by TEO with the AB in the absorption and transmission states as the objective functions. The specific optimized parameters are shown in Case 1 in Table 1.

The absorption state corresponds to μ_{c_1} = 0.0144 eV, and the absorption curves are depicted in Fig. 3(a). The ideal absorption is achieved within 7–15.45 THz. The AB is 8.45 THz, with RBW = 75.28%, indicating the realization of UWB absorption, which can be attributed to the perfect impedance matching between the MS and free space. Here, the theory of impedance matching is introduced to explain UBW absorption. The normalized surface impedance can be computed using eqn (23):[60]

$$\frac{Z_{\mathrm{eff}}}{Z_0} = Z_{\mathrm{r,eff}} + j \cdot Z_{\mathrm{i,eff}} = \frac{1+r}{1-r}, \quad (23)$$

where, Z_{eff} represents the effective surface impedance of this MS, and Z_0 denotes the vacuum wave impedance. The ratio of these two yields the normalized surface impedance, which can be divided into a real part $Z_{\mathrm{r,eff}}$ and an imaginary part $Z_{\mathrm{i,eff}}$. When the normalized surface impedance approaches 1, it indicates a perfect impedance match between the MS and free space. In this case, $Z_{\mathrm{r,eff}}$ approaches 1, $Z_{\mathrm{i,eff}}$ is nearly to be 0, and the reflection coefficient r approaches 0, suggesting that incident EWs are minimally reflected and mostly absorbed. The impedance matching curves for TE and TM waves are severally depicted in Fig. 3(b) and (c).

Between 7–15.45 THz, the impedance matching curves for TE and TM waves are highly similar, with the real parts approaching 1 and imaginary parts near 0, demonstrating the presence of UBW absorption in this region. However, on both sides of this interval, the impedance matching curves for TE and TM waves diverge differently, due to the anisotropy of InSb.[61] Consequently, both the real and imaginary parts exhibit strong oscillations near 1 and 0, respectively, leading to poorer absorption performance.

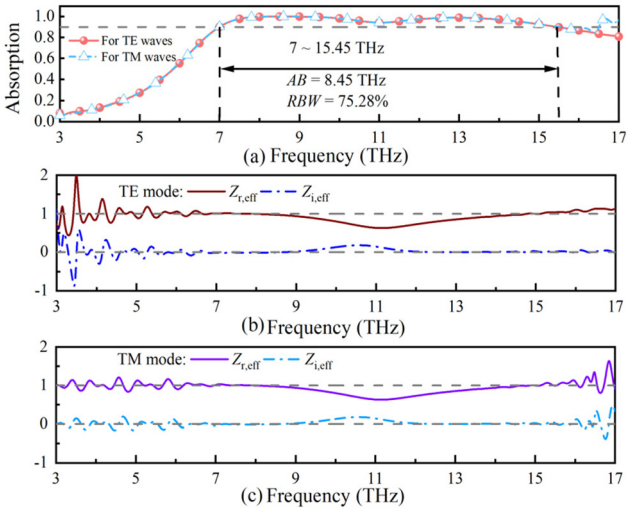

Fig. 3 (a) The spectra of absorption for such a MS. The plots of impedance matching for (b) TE waves, and (c) TM ones.

To further investigate the physical mechanism of UBW absorption, a frequency of 8.52 THz, corresponding to a peak absorptance of 99.97% for TE and TM waves, is selected for electric field distribution analysis. Since the absorptances of TE and TM waves are identical at 8.52 THz, only the electric field distribution under the TE mode is presented in Fig. 4. The currents primarily distribute within the sequence of $(\mathrm{GBGBG})^{N_1}$, on the left side of the MS. This is because the introduction of defect layers (B) in this sequence leads to energy localization, and the lower μ_c allows GHM to undergo intrinsic absorption, absorbing EWs. Therefore, it is hypothesized that the absorption functionality of MS is primarily accomplished by this sequence, and is independent of the sequence of $(\mathrm{AD})^{N_2}$.

When μ_c is modulated to 0.98 eV, the MS is switched to the transmission state. The results of transmissive LTC PC are shown in Fig. 5. The variation of AR in the frequency domain is displayed in Fig. 5(a). Within 3.9–15.58 THz, AR < 3 dB is achieved, indicating the realization of UBW PC. Fig. 5(b) presents the transmittance spectra of TE and TM waves. $T_{\mathrm{TM}} < 0.9$ only occurs below 3.8 THz, and $T_{\mathrm{TE}} < 0.9$ only exists within 15.32–17 THz, showing excellent transmittance performance. This can be attributed to the higher μ_c hindering electronic transitions within GHM, thereby suppressing the intrinsic absorption of EWs. Simultaneously, due to the excellent impedance matching between MS and the free space, EWs are seldom reflected and instead significantly pass through the MS. The $\Delta\varphi$ of the outgoing EWs is illustrated in Fig. 5(c),

Table 1 The structural information if this JM

	ε_A	ε_C	d_A (μm)	d_B (μm)	d_C (nm)	d_D (μm)	μ_{c_1} (eV)	μ_{c_2} (eV)	N_1	N_2
Case 1	1.32	3.5	6.55	6.3	20.65	0.046	0.0144	0.98	20	15
Case 2	1.16	2.68	7.89	8.44	20	0.072	0.016	0.992	25	10

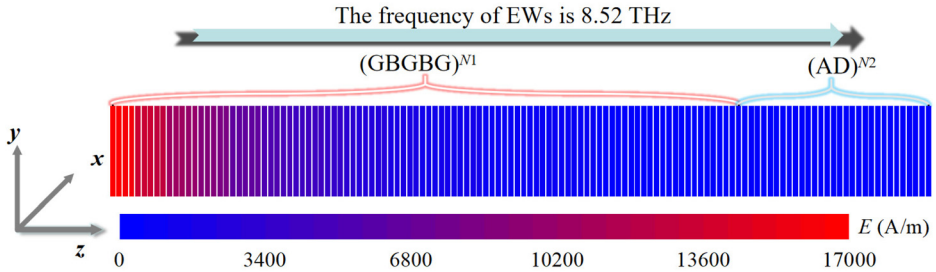

Fig. 4 The distribution of electric field of within the MS in the absorption state at a frequency of 8.52 THz.

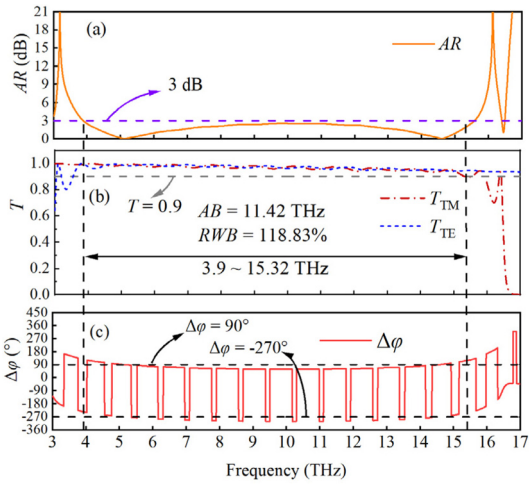

Fig. 5 In the transmission state, the transmissive PC is achieved with (a) displaying the AR, (b) showing the T_{TM} and T_{TE} and (c) indicating the $\Delta\varphi$.

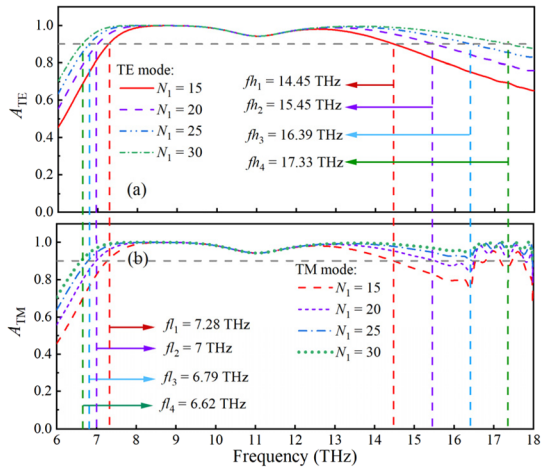

Fig. 6 The impacts of N_1 on the absorption for (a) TE and (b) TM modes.

which primarily alternates between approximately 90° and −270°, indicating that the transmitted EWs are right-handed circularly polarized. Overall, UWB transmissive LTC PC is achieved within 3.9–15.32 THz, corresponding to AB = 11.42 THz and RBW = 118.32%. The disparities in phase and transmittance observed between the outgoing TE and TM waves are due to the anisotropy of InSb. Functioning as a negative refractive index material, the periodic arrangement of InSb with the positively refractive index material A enables the outgoing EWs to maintain specific phases, consequently achieving PC.

Furthermore, since the period numbers N_1 and N_2 are crucial features of the MS, it is essential to investigate their impacts on both absorption and PC. Firstly, the influences of N_1 on the absorption bandwidth at normal incidence are discussed. The AB is given by AB = $f_h \times f_l$, where f_h and f_l severally represent the upper and lower cutoff frequencies. When N_1 is taken as 15, 20, 25, and 30, the corresponding lower cutoff frequencies are denoted as f_{l_1}, f_{l_2}, f_{l_3}, and f_{l_4}, respectively. Similarly, the corresponding upper cutoff frequencies are f_{h_1}, f_{h_2}, f_{h_3}, and f_{h_4}. The distinct influence of various N_1 on the absorption bandwidth is presented in Fig. 6. Specifically, Fig. 6(a) displays the absorption pattern for TE waves, while Fig. 6(b) illustrates the absorption behavior for the TM waves.

With the gradual increase in N_1, f_l progressively shifts from 7.28 THz to 6.62 THz, with the magnitude of this shift gradually reduced. And f_h has a blue shift, increasing from 14.45 THz to 17.33 THz. The AB and RBW both exhibit an increment. This phenomenon can be attributed to the augmentation of GHM layers with the increased N_1, resulting in a greater number of resonance peaks. The interaction and coupling of these numerous resonance peaks contribute to the broadening of the absorption spectrum. Compared Fig. 6(a) with Fig. 6(b), the absorption curves for TE and TM waves apparently remain consistent within 6–16 THz. However, deviations appear in the absorption curves beyond 16 THz. Specifically, beyond 16 THz, the absorptivity for TM waves surpasses that for TE waves, and the absorption curve exhibits oscillatory behavior. This is because of the anisotropic effect of InSb, resulting in enhanced absorption of EWs beyond 16 THz under the TM mode.

Furthermore, the impacts of gradually increasing N_2 from 5 to 20 on the absorption are depicted in Fig. 7, with Fig. 7(a) and (b) severally illustrating the absorption outcomes for TE and TM waves. The absorption curves for both waves closely align, displaying only minor disparities within 16–17 THz, which does not affect the magnitude of the absorption bandwidth. Different values of N_2 are represented by distinct colors

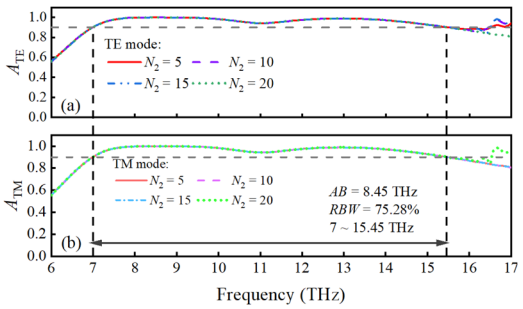

Fig. 7 The profiles of absorption curves for (a) TE and (b) TM waves, which are corresponding to various values of N_2.

on the absorption curves. Notably, variations in N_2 exhibit no influence on UWB absorption. The absorption interval remains within 7–15.45 THz, with AB maintaining at 8.45 THz, and the RBW measuring at 75.28%. Therefore, the absorption functionality of the MS is primarily governed by the $(GBGBG)^{N_1}$ segment.

Then the impacts of N_1 and N_2 on the bandwidth of the PC are investigated, with the MS switched to the transmission state. Firstly, by varying the value of N_1 while keeping the other conditions constant, the corresponding spectra of AR, T_{TM}, T_{TE}, and $\Delta\varphi$, are illustrated in Fig. 8(a)–(d), respectively. In Fig. 8, the variation of N_1 has a negligible influence on AR, T_{TM}, T_{TE}, and $\Delta\varphi$, resulting in the f_l of the PC bandwidth remaining at 3.9 THz. However, with N_1 increasing from 15 to 30, the bandwidth satisfying $T_{TM} > 0.9$ decreases, and the f_h lessens from 15.58 THz to 15.16 THz, leading to a decrease in AB from 11.68 THz to 11.26 THz, with the RBW fluctuating around 119%. This is because the increase in the number of GHM and defect layer (B) enhances the impedance matching between the MS and the environment, progressively improving the absorption capability and, consequently, reducing the transmission bandwidth. Overall, the changes of N_1 have little impact on the PC bandwidth. This is due to the symmetry of the $(GBGBG)^{N_1}$ sequence, which constrains the ability of incident EWs to rotate within the sequence, making it challenging for this sequence to influence PC effects.

Moreover, the impacts of N_2 on the PC are illustrated in Fig. 9. Specifically in Fig. 9(a), the AR is significantly influenced by N_2. However, in Fig. 9(b) and (c), the curves of T_{TE} and T_{TM} display minimal sensitivity to N_2 and their variations essentially have negligible effects on the changes in PC bandwidth. Hence, the primary factor influencing the bandwidth of the PC is the variation in AR. When N_2 is 5, the PC bandwidth is 0, with AR remaining consistently above 3 dB. As N_2 increases to 10, the PC bandwidth with AR < 3 dB expands to 2.54 THz, with a RBW of 56.2%, achieving UWB PC within 3.25–5.79 THz. Furthermore, as N_2 reaches 15, the PC bandwidth maximizes at 11.42 THz, accompanied by a max RBW of 118.8%. This is primarily due to the enhanced coupling effects of material A and InSb caused by the heightened N_2, which enhances the modulation of incident EWs, progressively amplifying the PC bandwidth. However, with N_2 escalated to 20, in Fig. 9(a), the AR curve corresponding to a bandwidth of less than 3 dB exhibits a blue shift in f_l and a red shift in f_h. This leads to a decrease in the PC bandwidth to 9.91 THz, and a reduction in RBW to 100.8%. This is because the mutual interaction between medium A and InSb at N_2 = 20, introduces additional phase difference to EWs, thereby affecting the

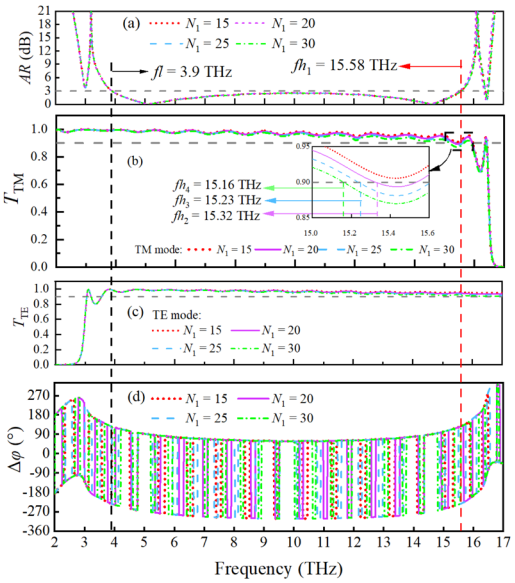

Fig. 8 The effects of N_1 on the transmissive PC with (a) displaying the AR, (b) depicting the T_{TM}, (c) showing the T_{TE} and (d) indicating the $\Delta\varphi$.

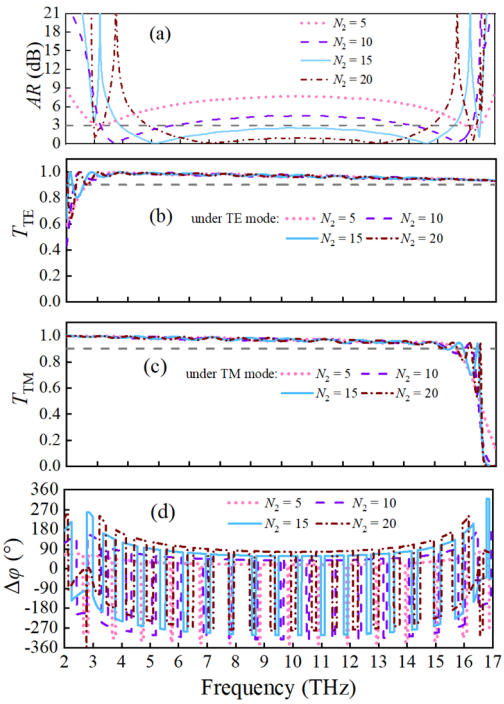

Fig. 9 The impacts of N_2 on the transmissive PC with (a) depicting AR, (b) showing the T_{TE}, (c) displaying the T_{TM}, and (d) indicating the $\Delta\varphi$.

efficiency of PC. The corresponding $\Delta\varphi$ curve is depicted in Fig. 9(d). Notably, at N_2 = 15 and 20, $\Delta\varphi$ predominantly fluctuates around −90° and 270°, corresponding to better PC bandwidths. Conversely, at N_2 = 5 and 10, $\Delta\varphi$ deviates from −90° and 270°, exhibiting poor phase matching conditions that lead to a smaller PC bandwidth. In summary, the variations in N_2 have a profound influence on the PC. Particularly, when N_2 is around 15, the PC bandwidth is maximum, achieving UWB PC. Consequently, it is signally that the PC functionality of the MS is predominantly realized by the sequence $(AD)^{N_2}$.

The preceding discussion has presented UWB absorption and transmissive LTC PC, however, all of which are established based on normal incidence conditions. The angular stability holds significant value across applications involving absorption and LTC PC. As a result, the research focus has shifted towards devising a tunable MS that is switchable between UWB absorption and PC with exceptional angular stability. With the angular stability optimized by TEO, a MS capable of toggling between large-angle absorption and transmissive PC is introduced. The specific structural parameters of this MS are outlined in Table 1, as the Case 2. The influences of diverse periodic numbers on its performance in achieving large-angle absorption and transmissive PC have been investigated. This comprehensive exploration provides valuable insights into balancing performance and manufacturing costs for this switchable MS.

Modulating the μ_c of the GHM to 0.016 eV, the MS exhibits large-angle absorption functionality. Given that the absorption functionality is primarily governed by the sequence $(GBGBG)^{N_1}$, the values of N_1 are set to 15, 20, 25, and 30, while keeping N_2 fixed at 15. The corresponding results for large-angle UWB absorption are illustrated in Fig. 10. To differentiate between the TE and TM modes, the incident angle is negative for TE waves, while that is positive for the TM waves. The region encompassed by solid black lines signifies absorptivity exceeding 0.9, indicative of the desired high absorption. Prioritizing the angular stability and bandwidth respectively leads to two distinct options. When the angular stability takes precedence, the optimized results are represented by the blue boxes in Fig. 10. For N_1 = 15, in Fig. 10(a), the corresponding absorption region entails AB = 3.2 THz and RBW = 28.3%. Under the TE mode, the angular stability reaches 75°, and it attains 60° under the TM mode. In Fig. 10(b) with N_1 = 20, under the same angular stability condition, AB expands to 3.6 THz, accompanied by a rise in RBW to 31.7%. Subsequently, in Fig. 10(c) at N_1 = 25, AB is 3.85 THz, with RBW = 31.2%. This corresponds to a maximum angular stability of 75° for TE waves and 65° for TM waves. Maintaining the same angular stability, as N_1 reaches 30, in Fig. 10(d), AB increases to 4.2 THz, while RBW reaches 38.2%, indicating the achievement of large-angle UWB absorption. The angular stability is found to be improved as N_1 increases. This can be attributed to the augmentation of the GHM and B, which enhances the multi-layer interference phenomenon at a specific frequency range for varying incident angles. Consequently, this reinforcement of absorption effects is observed across different angles.

When prioritizing the bandwidth, the ideal UWB absorption region is delineated by the purple boxes. For N_1 = 15 in Fig. 10(a), the max AB within 7–15 THz reaches 6.5 THz, corresponding to a RBW of 55.3%. Under the TE mode, the maximum absorption angle is 53°, whereas, under the TM mode, it is only 20°. While keeping the angular stability constant, as N_1 increases, the f_h remains at 15 THz, while the f_l gradually shifts from 8.5 THz to 7.6 THz, resulting in the gradual augmentation of both AB and RBW. In Fig. 9(d) when N_1 reaches 30, AB and RBW attain values of 7.4 THz and 65.5% respectively. Overall, the increase in N_1 enhances the impedance matching between the MS and free space, thereby elevating the absorption performance of the MS.

Altering the μ_c to 0.992 eV, the MS is switched to transmission state, demonstrating the large-angle transmissive LTC PC. As the PC functionality is primarily governed by $(AD)^{N_2}$, N_2 is set to be 5, 10, 15, and 20, while maintaining N_1 at 25, to examine the influence of N_2 on the angular stability of the PC. Since Fig. 9 establishes that AR is the chief factor affecting the bandwidth of transmissive PC, the impacts of N_2 on the angular stability of AR are initially explored, as depicted in Fig. 11. In Fig. 11, the regions satisfying AR < 3 dB are delineated by white circles, representing the realization of LTC PC. In Fig. 11(a) and (d), when N_2 is 5 and 20, respectively, the MS exhibits comparatively diminished PC performance. At N_2 = 5 in Fig. 11(a), the PC displays angle-insensitive behavior solely around 4 THz and 14 THz. For N_2 = 20 in Fig. 11(d), the PC predominantly manifests within 9–13 THz, accompanied by incident angle spanning from 50° to 65°. Notably, when N_2 is 10 or 15, the large-angle UWB PC is achieved, vividly portrayed in Fig. 11(b) and (c). Specifically, for N_2 = 15, at θ = 0°, within 5.86–12.66 THz, AR < 3 dB is satisfied. As θ escalates, both f_h

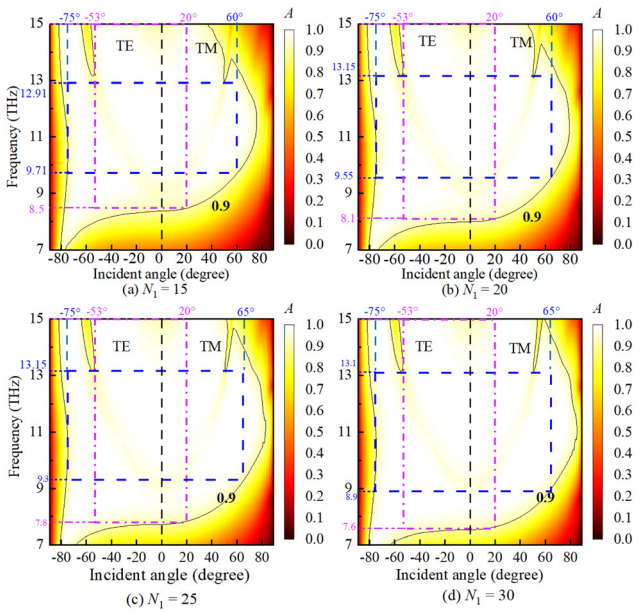

Fig. 10 The angle-insensitive absorption with (a) N_1 = 15, (b) N_1 = 20, (c) N_1 = 25, and (d) N_1 = 30.

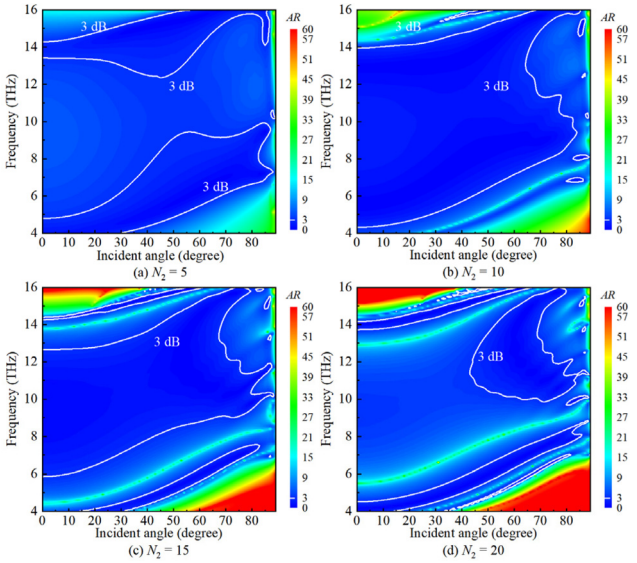

Fig. 11 The variation of AR with (a) N_2 = 5, (b) N_2 = 10, (c) N_2 = 15, and (d) N_2 = 20.

and f_l undergo a blue shift, yet f_l experiences a more pronounced shift, consequently causing a gradual reduction in the overall AB. At θ = 60°, AR < 3 dB is observed within 8.72–15.08 THz. For N_2 = 10, the area covered by AR < 3 dB is most favorable, indicating the best angular stability. At θ = 0°, AR < 3 dB is presented from 4.37 THz to 13.23 THz. Similar to the case of N_2 = 15, both f_h and f_l experience a blue shift, with an overall decrease in AB. When θ is 60°, AR < 3 dB emerges between 7.25 THz and 15.55 THz, displaying excellent angular stability of PC. Overall, the insufficient number of layers of the $(AD)^{N_2}$ leads to inadequate control over the passing EWs, while an excessive number of layers introduces additional phase differences that weaken the PC effect. N_2 = 10 corresponds to the best angular stability performance for AR.

When N_2 is 10, the variations of the transmittance and $\Delta\varphi$ with increasing incident angle for the MS in transmission state are severally illustrated in Fig. 12. In Fig. 12(a), to distinguish between TE and TM modes, the incident angle is negative for the TE waves, while the positive angle denotes the TM mode's incident angle. At θ = 0°, both T_{TE} and T_{TM} are greater than 0.9 within 4.47–13.03 THz. Under the TE mode, the transmittance between 4 to 5 THz is lower than that under the TM mode, while between 14 to 16 THz, the situation is reversed, which arises from the anisotropy of InSb. Overall, under both modes, the angular stability for T > 0.9 exceeds 60°, showcasing excellent angle-insensitive transmissive PC. Fig. 12(b) reveals that as the frequency and θ increase, $\Delta\varphi$ alternates between approximately 90° and −270°, signifying that the transmitted EWs are right-handed circularly polarized.

Conventional absorption devices lack controllability, which results in a fixed absorption range upon design completion, making them less adaptable to complex electromagnetic environments. Therefore, the tunability of the MS is of great importance. By applying a voltage to modulate the GHM's μ_c, the tunable absorption of the MS is achieved. Maintaining the other parameters in Case 1 unchanged, the variations of the absorption curves under TE and TM modes with various μ_c are presented in Fig. 13(a) and (b) at vertical incidence. The μ_c is set to 0.01 eV, 0.03 eV, 0.05 eV, and 0.07 eV respectively. Compared Fig. 13(a) with Fig. 13(b), the MS absorption curves under TE and TM modes exhibit consistency within 7–15 THz. However, some differences emerge within 15–18 THz. Particularly, at μ_c = 0.03 eV, a notable dissimilarity arises between TE and TM modes in the absorption behavior within 16.5–18 THz. Under the TM mode, absorption is significantly higher than that under the TE mode, which can be attributed to the absorption of TM waves by InSb. With an increase in μ_c, the f_l of the ideal absorption region, where A_{TE} and A_{TM} both exceed 0.9, experiences a blue shift. It moves from 7.71 THz to 13.61 THz. When μ_c is 0.01 eV, the ideal absorption achieves its maximum AB and RBW values of 8.71 THz and 72.2%, respectively. Conversely, with μ_c at 0.07 eV, the minimum values of AB and RBW are severally 2.61 THz and 17.5%. Generally, as μ_c increases, both AB and RBW gradually decrease. This arises from the elevated hindrance faced by electron transitions within GHM, caused by the heightened μ_c, which consequently dampens the intrinsic absorption of GHM. However, at μ_c = 0.03 eV, this decreasing trend is not observed. The corresponding AB = 4.15 THz is smaller than the μ_c = AB at 0.05 eV, which is 7.02 THz. This anomaly is

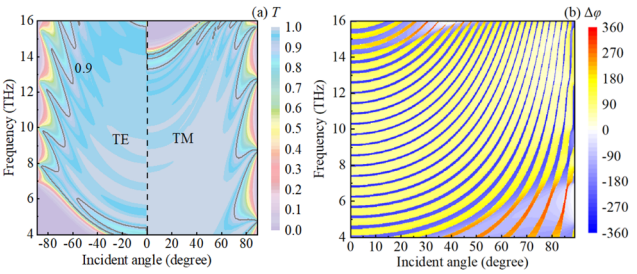

Fig. 12 The variation of (a) T with increasing incident angle, and (b) $\Delta\varphi$ with increasing incident angle.

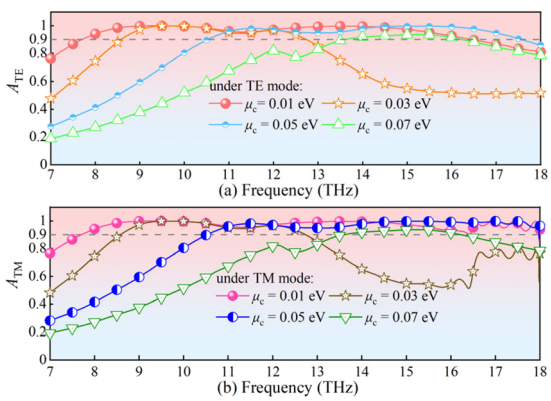

Fig. 13 The absorption curves with different values of μ_c for the (a) TE and (b) TM waves.

caused by the suboptimal impedance matching of the MS with the free space, leading to a red shift of f_h to 12.73 THz. Overall, varying μ_c yields distinct positions and magnitudes of ideal absorption intervals, demonstrating the flexible tunability of the MS absorption.

Furthermore, the connection between the μ_c and the absorption of EWs at different incident angles is also investigated. Maintaining the other parameters of Case 2 constant, μ_c is varied with values of 0.01 eV, 0.03 eV, 0.05 eV, and 0.07 eV. The corresponding absorption varying with θ is illustrated in Fig. 14.

At a μ_c value of 0.01 eV, Fig. 14(a) demonstrates the optimal angular stability within the absorption characteristics. Notably, the ideal absorption zone is concentrated between 10 to 14 THz, attaining an angular stability of 70° for TE waves and 60° for TM waves. As μ_c escalates, demonstrated across Fig. 14(b)–(d), the absorption zone gradually contracts while migrating toward higher frequency spectra. The emergence of a photonic band gap in Fig. 14 creates intervals that dissect the heightened absorption area, subsequently compromising angular stability. Broadly, heightened μ_c values correspond to diminished angular stability. Optimal angular stability is notably discernible at a μ_c of 0.01 eV. Additionally, varying the values of μ_c prompt shifts in the locations of the ideal absorption zones, thereby enabling the tunability of the absorption functionality.

In this paper, the magneto-optical medium InSb is introduced to achieve the PC function. Under the Voigt effect, the dielectric constant of the InSb exhibits tensor form. In the section of the calculation of the TMM, the TMM is derived by considering the effective refractive index of InSb, making it applicable for calculating multilayer periodic dielectric arrangements. To validate the accuracy and effectiveness of the results obtained using this approach, the TMM is derived based on the Voigt effect.[62] Subsequently, a comparative analysis is conducted between the results obtained from the two TMMs.

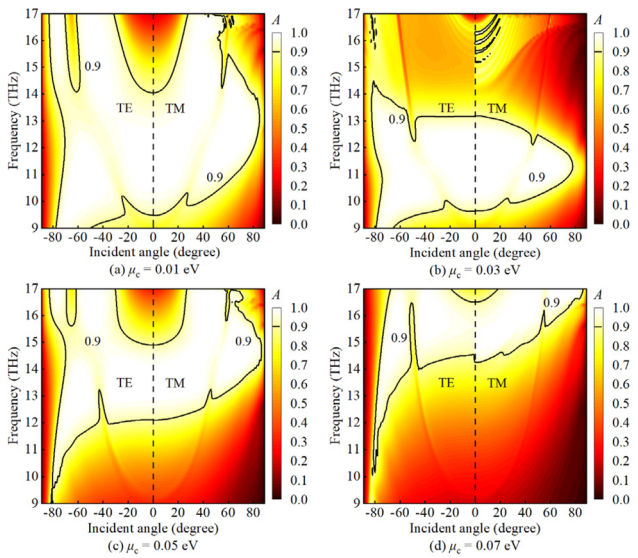

Fig. 14 The absorption diagrams of the MS with (a) μ_c = 0.01 eV, (b) μ_c = 0.03 eV, (c) μ_c = 0.05 eV and (d) μ_c = 0.07 eV.

Due to the complete decoupling of TM and TE modes in the Voigt geometry,[63] for the InSb, the property under the TE mode is exclusively influenced by the ε_{yy} component in the tensor, demonstrating isotropy. Consequently, the focus centers on the derivation of the TMM based on Voigt effect and the validation of the results under the TM mode. For the TM waves, under the Voigt effect, the dielectric tensor of magneto-optical medium InSb can be expressed as eqn (24):[62]

$$\hat{\boldsymbol{\varepsilon}}_i = \begin{pmatrix} \varepsilon & 0 & j\Delta \\ 0 & \varepsilon & 0 \\ -j\Delta & 0 & \varepsilon \end{pmatrix}, \tag{24}$$

where, ε represents ε_{xx}, and Δ is equivalent to ε_{xz}. Then the effective dielectric constant can be shown as eqn (25):[62]

$$\varepsilon' = \frac{\varepsilon^2 - \Delta^2}{\varepsilon}. \tag{25}$$

For ordinary materials, the Δ is 0. Hence, the derived method is equally applicable to media A, B, and G. Then the z and x components of wave vector of in the ith layer can be calculated as eqn (26) and (27) respectively:[62]

$$k_{zi} = \frac{\omega}{c} \cdot \sqrt{\varepsilon'_i} \cdot \cos\theta_i, \quad (i = \mathrm{A}, \mathrm{D}, \mathrm{G}, \mathrm{B}), \tag{26}$$

$$k_{xi} = \frac{\omega}{c} \cdot \sqrt{\varepsilon'_i} \cdot \sin\theta_i, \quad (i = \mathrm{A}, \mathrm{D}, \mathrm{G}, \mathrm{B}). \tag{27}$$

The usual propagation matrix $\boldsymbol{P}_i$ of ith layer can be obtained as eqn (28):[62]

$$\boldsymbol{P}_i = \begin{pmatrix} e^{ik_{zi}di} & 0 \\ 0 & e^{-ikzidi} \end{pmatrix}, \quad (i = \mathrm{A}, \mathrm{D}, \mathrm{G}, \mathrm{B}). \tag{28}$$

The dynamical matrix $\boldsymbol{T}_{ij}$, guiding EWs transmission through the interface from layer i to layer j, is illustrated in eqn (29):[62]

$$\boldsymbol{T}_{ij} = \frac{1}{2N_i}\begin{pmatrix} N_i - M_i + N_j + M_j & N_i - M_i - N_j + M_j \\ N_i + M_i - N_j - M_j & N_i + M_i + N_j - M_j \end{pmatrix}, \quad (i,j = \mathrm{A}, \mathrm{D}, \mathrm{G}, \mathrm{B}), \tag{29}$$

where the $M_{j(i)} = [-ik_{xj(i)}\Delta_{j(i)}]/[\varepsilon_{j(i)}\varepsilon'_{j(i)}]$ and $N_{j(i)} = ik_{zj(i)}/\varepsilon'_{j(i)}$. Eventually, the complete transmission matrix of the entire MS in an air background can be depicted as eqn (30)

$$\begin{aligned} \mathbf{M} = {} & T_{0G}(P_G T_{GB} P_B T_{BG} P_G T_{GB} P_B T_{BG} P_G T_{GG})^{N_1 - 1} \\ & P_G T_{GB} P_B T_{BG} P_G T_{GB} P_B T_{BG} P_G T_{GA} (P_A T_{AD} P_D T_{DA})^{N_2 - 1} \\ & P_A T_{AD} P_D T_{D0}. \end{aligned} \tag{30}$$

Then the transmission coefficient t and reflection coefficient r of the EWs through the MS can be computed as $t = 1/\mathbf{M}(1,1)$ and $r = \mathbf{M}(2,1)/\mathbf{M}(1,1)$ respectively, and the transmittance, reflectance and absorptivity of the EWs can be obtained.

For simplicity, validation has been performed solely on the absorption and PC results under normal incidence for Case 1

in Table 1. The angular-insensitive UWB absorption and PC corresponding to the condition of Case 2 in Table 1 can also be validated using the TMM based on the Voigt effect.

Specifically, in the absorption state, the comparison between the calculated UWB absorption using the TMM based on the Voigt effect and the original simulation results is illustrated in Fig. 15. In Fig. 15, the absorption performance obtained by the TMM based on the Voigt effect closely aligns with the original results, validating the reliability and reasonability of the simulation outcomes.

Additionally, in the transmission state, the PC results calculated by the TMM based on the Voigt effect and the original results are illustrated in Fig. 16. In Fig. 16(b), the transmittance obtained from TMM based on the Voigt effect is slightly lower than the original results within 3–16 THz, while remaining consistent within 16–17 THz. This is because the original method ultilizing the equivalent refractive index of InSb, overlooks a negligible loss factor, resulting in slightly higher simulated transmittance. However, in Fig. 16(a) and (c), the curves of AR and $\Delta\varphi$ obtained by the two calculation methods exhibit a high level of consistency, demonstrating the reliability and validity of the original simulation results.

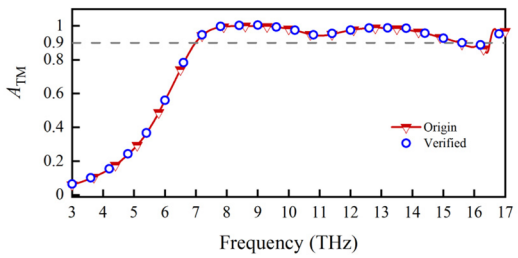

Fig. 15 The comparison between the origin absorption results and that obtained by TMM based on Voigt effect.

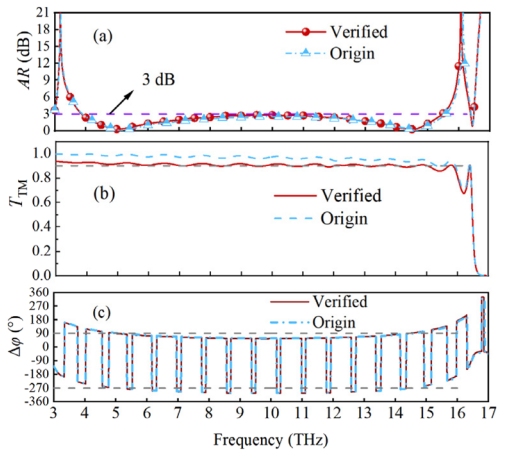

Fig. 16 The comparison of the verified PC results and the origin outcomes, with (a) showing the AR, (b) displaying the T_{TM} and (c) exhibiting the $\Delta\varphi$.

Table 2 Thecomparison between the optimized MS and existing absorbers and LTC polarization converters

		For absorption ($A > 0.9$)				For LTC PC (AR < 3 dB)			
Ref.	Function	Absorption interval	AB	RBW	Angular stability	Type	Interval of PC (AR < 3 dB)	AB	RBW	Angular stability
12	Absorption	0.38–0.71 THz	0.33 THz	60%	45°	×	×	×	×	×
14	Absorption	3–7.8 THz	4.8 THz	88.8%	50° for TM modes only	×	×	×	×	×
19	Absorption	2.34–5.64 THz	3.3 THz	82.7%	55° ($A > 0.75$)	×	×	×	×	×
20	Absorption	1.54–2.12 THz	0.58 THz	31.69%	×	×	×	×	×	×
27	PC	×	×	×	×	Reflection ($R > 0.7$)	0.6–1.41 THz	0.81 THz	80%	20°
29	PC	×	×	×	×	Transmission ($T > 0.7$)	8–12 GHz	4 GHz	40%	45°
30	PC	×	×	×	×	Transmission ($T > 0.9$)	17.6–22.4 GHz	4.8 GHz	24%	50°
31	PC	×	×	×	×	Transmission ($T > 0.88$)	0.555–0.737 THz	0.182 THz	28.17%	×
32	PC	×	×	×	×	Transmission ($T > 0.82$)	0.46–0.62 THz	0.16 THz	29.6%	×
33	Absorption and PC	0.74–1.62 THz	0.87 THz	75%	35° for TE mode only	Reflection	1.47–2.27 THz	0.8 THz	42.7%	50°
Case 1 in this work	Absorption and PC	7–15.45 THz	8.45 THz	75.28%	×	Transmission ($T > 0.9$)	3.9–15.32 THz	11.42 THz	118.8%	×
Case 2 in this work	Absorption and PC	8.9–13.1 THz	4.2 THz	38.2%	TE: 75° and TM: 65°	Transmission ($T > 0.9$)	4.37–13.23 THz	8.86 THz	100.7%	60°

Eventually, a comparison between the optimized MS and the existing absorbers and polarization converters is summarized in Table 2. The proposed MS not only integrates the functionalities of absorption and transmissive LTC PC but also exhibits significant advantages in bandwidth, angular stability, and transmittance of PC, rendering it capable of flexibly adapting to even more intricate electromagnetic environments.

4. Conclusion

In this paper, an optimized MS switchable between UWB angle-insensitive absorption and transmissive LTC PC is proposed. The manipulation of a bias voltage to regulate the μ_c of the GHM enables the MS to seamlessly transition between absorption and transmission states. In the absorption state, at normal incidence, within 7–15.45 THz, the UWB absorption is achieved, featuring an AB of 8.45 THz and a RBW of 75.28%. When emphasizing the angular stability, angle-insensitive absorption is realized from 8.9 THz to 13.1 THz. Notably, the angular stability extends to 75° for TE waves and 65° for TM waves. In the transmission state, focusing solely on normal incidence, the UWB LTC PC is achieved within 3.9–15.32 THz. The optimized AB measures 11.42 THz, with a RBW of 118.8%. When accounting for oblique incidence, the MS exhibits angle-insensitive PC within 4.37–13.23 THz, corresponding to an AB of 8.86 THz and a RBW of 100.7%. The incident angular stability reaches 60°. By analyzing the distribution of electric fields and investigating the impacts of the period number N_1 and N_2 on the performance of the MS, the roles of each sequence within the MS are explored. It is observed that N_1 and N_2 have distinct effects on absorption and PC. Ultimately, by manipulating the μ_c of the GHM, the tunability of UWB absorption is achieved. This MS possesses a synergistic capability to handle multiple functions, offering advantages such as ultra-wide operating frequency, exceptional angular stability, and flexible control. It can serve as a valuable reference for designing multifunctional devices and holds immense potential for applications in fields such as stealth technology, radar cross-section reduction, communication systems, and electromagnetic pollution management.

Conflicts of interest

The authors declare no conflict of interest.

Acknowledgements

This work was supported by the College Student Innovation Training Program of Nanjing University of Posts and Telecommunications.

References

1 P. Hillger, J. Grzyb, R. Jain and U. R. Pfeiffer, *IEEE Trans. Terahertz Sci. Technol.*, 2018, **9**, 1–19.
2 G. Valušis, A. Lisauskas, H. Yuan, W. Knap and H. G. Roskos, *Sensors*, 2021, **21**, 4092.
3 D. M. Mittleman, *Opt. Express*, 2018, **26**, 9417–9431.
4 H. Tian, G. Huang, F. Xie, W. Fu and X. Yang, *TrAC, Trends Anal. Chem.*, 2023, 117057.
5 M. S. Khan, G. Varshney and P. Giri, *IEEE Trans. NanoBiosci.*, 2021, **20**, 488–496.
6 H.-J. Song and N. Lee, *IEEE Trans. Terahertz Sci. Technol.*, 2021, **12**, 105–117.
7 I. F. Akyildiz, J. M. Jornet and C. Han, *Phys. Commun. Commun.*, 2014, **12**, 16–32.
8 A. Ahmadivand, B. Gerislioglu and Z. Ramezani, *Nanoscale*, 2019, **11**, 8091–8095.
9 M. Mansouree, H. Kwon, E. Arbabi, A. McClung, A. Faraon and A. Arbabi, *Optica*, 2020, **7**, 77–84.
10 H. Xiong and Q. Shen, *Nanoscale*, 2020, **12**, 14598–14604.
11 W. Zhu, R. Yang, Y. Fan, Q. Fu, H. Wu, P. Zhang, N.-H. Shen and F. Zhang, *Nanoscale*, 2018, **10**, 12054–12061.
12 C. Du, D. Zhou, H.-H. Guo, Y.-Q. Pang, H.-Y. Shi, W.-F. Liu, J.-Z. Su, C. Singh, S. Trukhanov and A. Trukhanov, *Nanoscale*, 2020, **12**, 9769–9775.
13 Y. Li, W. Gao, L. Guo, Z. Chen, C. Li, H. Zhang, J. Jiao and B. An, *Opt. Express*, 2021, **29**, 41222–41233.
14 Z. Xu, D. Wu, Y. Liu, C. Liu, Z. Yu, L. Yu and H. Ye, *Nanoscale Res. Lett.*, 2018, **13**, 1–8.
15 J. Liu, M. Zhu, N. Zhang, H. Zhang, Y. Zhou, S. Sun, N. Yi, S. Gao, Q. Song and S. Xiao, *Nanoscale*, 2015, **7**, 18914–18917.
16 D. Wang, K.-D. Xu, S. Luo, Y. Cui, L. Zhang and J. Cui, *Nanoscale*, 2023, **15**, 3398–3407.
17 Z. Chen, P. Cai, Q. Wen, H. Chen, Y. Tang, Z. Yi, K. Wei, G. Li, B. Tang and Y. Yi, *Electronics*, 2023, **12**, 2655.
18 Y. He, Q. Wu and S. Yan, *Plasmonics*, 2019, **14**, 1303–1310.
19 G. Wu, X. Jiao, Y. Wang, Z. Zhao, Y. Wang and J. Liu, *Opt. Express*, 2021, **29**, 2703–2711.
20 B.-X. Wang, C. Xu, H. Zhou and G. Duan, *APL Mater.*, 2022, **10**, 050701.
21 J. Yang, S. T. Chen, M. Chen, J. C. Ke, M. Z. Chen, C. Zhang, R. Yang, X. Li, Q. Cheng and T. J. Cui, *IEEE Trans. Antennas Propag.*, 2020, **69**, 806–814.
22 W. Li, S. Gao, Y. Cai, Q. Luo, M. Sobhy, G. Wei, J. Xu, J. Li, C. Wu and Z. Cheng, *IEEE Trans. Antennas Propag.*, 2017, **65**, 4470–4477.
23 W. Xu, P. Li and Y. Qiu, *IEEE Antennas Wirel. Propag. Lett.*, 2018, **18**, 74–78.
24 R. Verre, N. Maccaferri, K. Fleischer, M. Svedendahl, N. O. Länk, A. Dmitriev, P. Vavassori, I. V. Shvets and M. Käll, *Nanoscale*, 2016, **8**, 10576–10581.
25 D. Gangwar, S. Singh, A. Sharma, S. P. Singh and A. Lay-Ekuakille, *Sens. Actuators, A*, 2022, **333**, 113273.

26 Y. Fu, Y. Wang, G. Yang, Q. Qiao and Y. Liu, *Opt. Express*, 2021, **29**, 13373–13387.
27 Y. Jiang, L. Wang, J. Wang, C. N. Akwuruoha and W. Cao, *Opt. Express*, 2017, **25**, 27616–27623.
28 R. Orr, G. Goussetis, V. Fusco and E. Saenz, *IEEE Trans. Antennas Propag.*, 2015, **63**, 1949–1956.
29 F. A. Dicandia and S. Genovesi, *IEEE Antennas Wirel. Propag. Lett.*, 2022, **21**, 2191–2195.
30 E. Arnieri, F. Greco and G. Amendola, *IEEE Trans. Antennas Propag.*, 2020, **69**, 578–583.
31 Y. Hou, C. Zhang and C. Wang, *IEEE Access*, 2020, **8**, 140303–140309.
32 J. Wu, M. A. S. Syed, L. Qi, X. Tao, J. Yang and L. Wen, *J. Appl. Phys.*, 2022, **132**, 013103.
33 D. Yan, M. Meng, J. Li, J. Li and X. Li, *Opt. Express*, 2020, **28**, 29843–29854.
34 T. Wang, H. Zhang, Y. Zhang, Y. Zhang and M. Cao, *Opt. Express*, 2020, **28**, 17434–17448.
35 S. Biswas, M. Y. Grajower, K. Watanabe, T. Taniguchi and H. A. Atwater, *Science*, 2021, **374**, 448–453.
36 B. Deng, R. Frisenda, C. Li, X. Chen, A. Castellanos-Gomez and F. Xia, *Adv. Opt. Mater.*, 2018, **6**, 1800365.
37 A. Gevorgyan, M. Harutyunyan, G. Matinyan, K. Oganesyan, Y. V. Rostovtsev, G. Kurizki and M. Scully, *Laser Phys. Lett.*, 2016, **13**, 046002.
38 S.-T. Xu, F. Fan, Y.-Y. Ji, J.-R. Cheng and S.-J. Chang, *Opt. Lett.*, 2019, **44**, 2450–2453.
39 Z. Song and J. Zhang, *Opt. Express*, 2020, **28**, 12487–12497.
40 Z. Peng, Z. Zheng, Z. Yu, H. Lan, M. Zhang, S. Wang, L. Li, H. Liang and H. Su, *Opt. Laser Technol.*, 2023, **157**, 108723.
41 Q. Xie, J. Sun, C. Su, F. Xia, M. Wang, K. Zhang and M. Yun, *Diamond Relat. Mater.*, 2023, 110119.
42 S. Zhang, Z. Li and F. Xing, *Int. J. Mol. Sci.*, 2020, **21**, 1608.
43 Y. Kang and H. Liu, *Superlattices Microstruct.*, 2018, **114**, 355–360.
44 M. A. Othman, C. Guclu and F. Capolino, *Opt. Express*, 2013, **21**, 7614–7632.
45 A. N. Grigorenko, M. Polini and K. Novoselov, *Nat. Photonics*, 2012, **6**, 749–758.
46 A. Kaveh and A. Dadras, *Adv. Eng. Softw.*, 2017, **110**, 69–84.
47 L. Qi, Z. Yang, F. Lan, X. Gao and Z. Shi, *Phys. Plasmas*, 2010, **17**, 042501.
48 F. Wu, D. Liu, H. Li and M. Feng, *Phys. Chem. Chem. Phys.*, 2023, **25**, 10785–10794.
49 M. Amin, M. Farhat and H. Bağcı, *Opt. Express*, 2013, **21**, 29938–29948.
50 X. Gao, W. Yang, W. Cao, M. Chen, Y. Jiang, X. Yu and H. Li, *Opt. Express*, 2017, **25**, 23945–23954.
51 X. Yuan, J. Chen, J. Wu, X. Yan, Y. Zhang and X. Zhang, *Results Phys.*, 2022, **37**, 105571.
52 F. Jabbarzadeh, M. Heydari and A. Habibzadeh-Sharif, *Mater. Res. Express*, 2019, **6**, 086209.
53 A. Andryieuski and A. V. Lavrinenko, *Opt. Express*, 2013, **21**, 9144–9155.
54 B. Wang, S. Eichfield, D. Wang, J. Robinson and M. Haque, *Nanoscale*, 2015, **7**, 14489–14495.
55 A. Pianelli, R. Kowerdziej, M. Dudek, K. Sielezin, M. Olifierczuk and J. Parka, *Opt. Express*, 2020, **28**, 6708–6718.
56 C. Guclu, S. Campione and F. Capolino, *Phys. Rev. B: Condens. Matter Mater. Phys.*, 2012, **86**, 205130.
57 F. Fan, S.-J. Chang, W.-H. Gu, X.-H. Wang and A.-Q. Chen, *IEEE Photonics Technol. Lett.*, 2012, **24**, 2080–2083.
58 J. Shabanpour, S. Beyraghi and H. Oraizi, *Sci. Rep.*, 2020, **10**, 14920.
59 B. Lin, J.-l. Wu, X.-y. Da, W. Li and J.-j. Ma, *Appl. Phys. A*, 2017, **123**, 1–5.
60 Y. Huang, J. Ji, Y. Chen, X. Li, J. He, X. Cheng, S. He, Y. Liu and J. Liu, *Composites, Part B*, 2019, **163**, 598–605.
61 J. Zhao, N. Li and Y. Cheng, *Opt. Commun.*, 2023, **536**, 129372.
62 Y.-t. Fang, Y.-x. Ni, H.-q. He and J.-x. Hu, *Opt. Commun.*, 2014, **320**, 99–104.
63 H. Y. Dong, J. Wang and T. J. Cui, *Phys. Rev. B: Condens. Matter Mater. Phys.*, 2013, **87**, 045406.

